

# Infrared Nanoscopy and Tomography of Intracellular Structures

**Katerina Kanevche**

FU Berlin

**David Burr**

FU Berlin

**Andreas Elsaesser**

FU Berlin

**Pascal-Kolja Hass**

FU Berlin

**Dennis Nuernberg**

FU Berlin

**Joachim Heberle** (✉ [jheberle@zedat.fu-berlin.de](mailto:jheberle@zedat.fu-berlin.de))

FU Berlin

---

## Research Article

**Keywords:** sSNOM, IR spectroscopy, nanoFTIR, fluorescence, super-resolution imaging

**Posted Date:** July 26th, 2021

**DOI:** <https://doi.org/10.21203/rs.3.rs-753486/v1>

**License:**   This work is licensed under a Creative Commons Attribution 4.0 International License.

[Read Full License](#)

---

# Abstract

The few microscopic techniques that simultaneously gather morphological and chemical data often rely on the use of specific markers. To eliminate this flaw, we have developed a method of examining cellular cross sections using the imaging power of scattering-type scanning near-field optical microscopy and Fourier-transform infrared spectroscopy at a spatial resolution far beyond the diffraction limit. Herewith, nanoscale surface and volumetric chemical imaging is performed using the intrinsic contrast generated by the characteristic absorption of mid-infrared radiation by the covalent bonds. We employ infrared nanoscopy to study the subcellular structures of eukaryotic (*Chlamydomonas reinhardtii*) and prokaryotic (*Escherichia coli*) species, revealing chemically distinct regions within each cell such as the microtubular structure of the flagellum. Serial 100 nm-thick cellular cross-sections were compiled into a tomogram yielding a three-dimensional infrared image of subcellular structure distribution at 20 nm resolution. The presented methodology is able to image biological samples competing current fluorescence nanoscopy but at less interference due to the low energy of infrared radiation and the absence of labeling.

## Introduction

Cutting edge single-cell techniques can allow for highly precise detection of subcellular components. Observation of the molecular composition of such organelles provides further understanding of their underlying biological processes, cellular mechanics and structural interactions. The visualization of subcellular components is commonly achieved by fluorescence or electron microscopy (EM). Despite the resolving power of cryoEM [1], this method provides little to no information about the chemical composition of the sample. In contrast, colorimetric or fluorescent markers chemically interact with specific cellular components, and thus can produce particularly detailed images of complex intracellular structures [2]. Although fluorescence-based super-resolution microscopy offers the possibility to perform biological and biomedical imaging beyond the diffraction limit and has potential to be furthered by novel technological developments [3], fluorescence imaging remains reliant on the use of chemically-specific labels.

Vibrational spectroscopy and microscopy overcome this barrier, performing chemical imaging in a label-free manner. The sensitivity and speed of infrared (IR) microscopic imaging of biological samples has been dramatically improved by the introduction of the novel quantum cascade lasers (QCLs) [4], [5]. Yet, diffraction limits the lateral resolution of IR microscopy to the  $\mu\text{m}$  range and is, thus, less applicable to examining subcellular components. Spectroscopic techniques that utilize Raman scattering, such as coherent anti-Stokes or stimulated Raman scattering can provide subcellular images at a spatial resolution down to 130 nm [6]. However, due to the high-intensity light source required, Raman spectroscopy is often damaging to biological samples. In contrast, scattering-type scanning near-field optical microscopy (sSNOM) integrates the resolving power of atomic force microscopy (AFM) with the molecular specificity and non-destructive nature of IR spectroscopy. The lateral resolution of sSNOM is not wavelength dependent [7], but dictated by the size of the microscopy probe tip [8], and thus can yield IR images at a resolution down to 5 nm [9]. Employing a broadband IR laser in an interferometric scheme

produces nanometer-resolution IR absorption spectra via Fourier-transformed IR spectroscopy (nanoFTIR) [10]. Thus, sSNOM and nanoFTIR present particularly powerful tools for performing molecularly specific measurements of biologically relevant systems, such as single protein complexes [11], individual amyloid fibrils [12] and lipids [13]. In addition to measurements on thin and well defined surfaces, sSNOM and nanoFTIR have been used for the imaging and spectroscopy of whole cells [14]. The information gathered via traditional sSNOM and nanoFTIR is however limited to a few tens of nm below the sample surface [15]. Therefore, when examining whole cells, internal structures remain obscured by the cell wall or membrane.

Our present work describes a nanoscopic technique that applies the super-resolution imaging power and spectroscopic strengths of sSNOM and nanoFTIR to cellular cross sections, prepared by a method well-established in EM. Combining the strengths of these techniques allows for nanoscale resolution, intracellular near-field IR imaging and spectroscopy, to be employed on 100 nm thick sections of both a prokaryotic and eukaryotic model species. Other recent approaches have applied AFM and nanoFTIR on cross-sectioned plant cells [16]. However, our study expands on the use of mid-IR illumination to report the local protein distribution of internal cellular organelles. Additionally, multiple sequential cross-sections of the same cell were examined, allowing for 3D reconstruction of cellular spectroscopic tomography. This approach enables the detection and visualization of the chemical composition of individual microorganisms and their subcellular components in a non-invasive manner, without the need to include highly specific, potentially artefact-inducing or hazardous sample staining, which can be expanded to imaging of multicellular structures and tissues. Ultimately, IR nanoscopy is able to resolve single protein complexes of a cell as demonstrated in the present work.

## Results

### NanoFTIR and sSNOM operating principle

Near-field nanoscopy was performed by focusing IR radiation on a metallic AFM tip, generating a confined near field at the tip's apex [17] (Figure 1a). When the sample is brought close to the tip, light is scattered from the tip and carries information on the optical properties of the surface beneath the tip, where the scattered amplitude relates to the reflectivity and the phase to the absorption of the surface [18]. Essentially, the AFM tip acts as point source of light. As a consequence, optical resolution is defined by the diameter of the tip apex but not by the wavelength. The weak intensity of the scattered photons and the low performance of IR detectors as compared to highly sensitive UV/Vis detectors, is effectively compensated by lock-in detection where the oscillating AFM cantilever provides the carrier frequency for detection. In sSNOM imaging mode, the surface is raster scanned at a single frequency of the QCL in pseudoheterodyne detection scheme [19], thus simultaneously obtaining AFM topography, near-field amplitude and phase images (Figure 1b). For nanoFTIR spectroscopy, a difference frequency generation-based fs laser [20] is used to illuminate the tip with broadband IR radiation. The scattered light is fed into a Michelson interferometer and a near-field IR absorption spectrum is recorded at each tip position [21] (Figure 1c).

## Subcellular nanoFTIR spectroscopy

The morphology of *Chlamydomonas reinhardtii* (Figure 2) and *Escherichia coli* (Figure S1) thin sections were investigated using TEM as a reference to compare against AFM images. Several distinct subcellular features and organelles were identifiable [22] with both TEM (Figure 2a) and AFM (Figure 2b), including the nucleus and nucleolus, the photosystem-containing thylakoid membranes, the pyrenoid with its distinctive starch inclusions, and the exterior plasma membrane.

Using nanoFTIR, locally resolved spectra were recorded on several intracellular locations as well as on the cell-free region containing only the embedding resin (Figure 2c). Each spectrum was measured on a single spot with size given by the AFM tip radius at lateral resolution of 20 nm (Figure S3d), marked on the AFM micrograph and referenced against a spectrum recorded on bare Au surface. The spectral region between 1800 and 1500  $\text{cm}^{-1}$  demonstrates multiple characteristic absorption features that vary with different measuring positions (Figure 2c). Spectrum #1 (black) was measured on a cell-free region and the dominant peak at 1738  $\text{cm}^{-1}$  corresponds to the C=O stretching vibration of succinic anhydride present in the epon-like embedding resin. Spectrum #2 (blue) was recorded on the central part of the pyrenoid. It shows distinct absorption peaks at 1655  $\text{cm}^{-1}$ , assigned to the C=O stretch of amide, and 1540  $\text{cm}^{-1}$  stemming from combined N-H bending and C-N stretching modes, known as amide I and amide II, respectively [11]. These peaks indicate high protein content and, as previously reported, the pyrenoid is largely composed of polypeptides such as RuBisCO [23], [24], the key enzyme involved in  $\text{CO}_2$  fixation. Spectrum #3 (purple) recorded in the nuclear region is dominated by similar absorption of bands at 1655  $\text{cm}^{-1}$  and 1540  $\text{cm}^{-1}$  suggesting protein content in this region. Yet, the IR bands of DNA (characterized by ring modes of purine and pyrimidine [25], [26]) are likely to contribute to this absorption spectrum as well. Spectrum #4 (pink) corresponds to the local IR absorption of the thylakoid with prominent amide I and amide II absorption bands due to the high protein content of the large photosynthetic complexes Photosystem I (PSI) and Photosystem II (PSII) contained within. Additional contributions in the 1560  $\text{cm}^{-1}$  and 1520  $\text{cm}^{-1}$  regions may be due to the C=O and C=N vibrations of chlorin rings, typical of chlorophyll [27] in PSI and PSII. The low intensity peak at around 1740  $\text{cm}^{-1}$  could be related to either chlorophyll or the resin. The cytoplasmic inner region was probed at several locations, each producing similar spectra as observed in the resin (Figure 2c, spectra #5, #6 and #7), thus indicating resin penetration inside of the cell. In contrast, spectrum #8 (green) has almost no resin absorption but shows distinct amide I and amide II peaks. This suggests that although measured on a visually similar cellular location to spectra #5 – 7, this spectrum was recorded from a protein-rich organelle. Finally, spectrum #9 (cyan) was taken from the very edge of the cell in order to observe the plasma membrane. However, as the dominant absorption peak at 1738  $\text{cm}^{-1}$  may originate from C=O stretching vibrations of either the membrane lipids or the resin, the assignment remains ambiguous. To gain insight into the near-field absorption at lower wavenumbers, additional measurements were performed covering spectral region down to  $\sim 1000 \text{ cm}^{-1}$  (Figure S2) to probe molecular vibrations of phosphate and ribose groups of DNA originating from the nucleus.

## Single-wavelength sSNOM imaging

Based on our nanoFTIR analysis, we recorded sSNOM images at specific marker wavenumbers. The AFM topography of the selected cell (Figure 3a) is visually similar to the previously examined sections (Figure 2a and b), with several distinct morphological features present. Phase-contrast imaging at  $1738\text{ cm}^{-1}$  (Figure 3b) shows strong absorption in the area surrounding the cell and in several, well-defined intracellular vacuoles, reinforcing the previous identification of the  $1738\text{ cm}^{-1}$  absorption band being primarily due to the embedding resin.

In contrast, Figures 3c and d show a near complete visual inversion with a uniform lack of absorption across all areas that the resin is present. Similar to nanoFTIR observations (Figure 2c), visualization at the wavenumbers corresponding to amide I ( $1655\text{ cm}^{-1}$ , Figure 3c) and amide II ( $1540\text{ cm}^{-1}$ , Figure 3d) both show strong absorption across several cellular features, including the pyrenoid, the chloroplast and the nuclear region. Interestingly, absorption at  $1540\text{ cm}^{-1}$  is relatively homogenous across the nucleus (Figure 3d), whereas absorption at  $1655\text{ cm}^{-1}$  provides a higher-contrast image, allowing for the nucleolus to be clearly distinguished from the surrounding nuclear area (Figure 3c). This increase in intensity is likely the result of the high density of proteins, nucleobases and other genetic material in this region.

Imaging at  $1238\text{ cm}^{-1}$  showed low overall absorption (Figure 3e) with the exception of several small but clearly resolved regions within the cytoplasm. However, imaging at this wavenumber allowed for clear visualization of the thylakoid stacks within the chloroplast. Also, the nucleolus is distinguishable from the nucleus with a slight increase in absorption likely due to the asymmetric P-O stretching vibration of phosphate. Cellular imaging at  $1155\text{ cm}^{-1}$  (Figure 3f) resembles the absorption pattern seen at  $1738\text{ cm}^{-1}$  (Figure 3b), showing strong absorption on the resin area outside the cell and within cellular vacuoles. Visualization at  $1155\text{ cm}^{-1}$  provides additional contrast, particularly of the thylakoid membranes and the protrusions in and around the pyrenoid. This adds further evidence to the assignment of this absorption feature as C-O-C stretching vibrations, present in a mixture of complex carbohydrates (such as starch) and the embedding resin.

In addition to AFM morphology and sSNOM phase contrast, information on the local reflectivity was gathered via sSNOM scattering amplitude. Several intracellular structures are depicted (Figure 4), demonstrating both the resolving power of sSNOM imaging and the potential of these imaging modes to each reveal different cellular features. While the cell wall was indistinct when imaged with AFM (Figure 4a), it is readily apparent when visualized with either amide I phase contrast (Figure 4b) or scattering amplitude (Figure 4c), appearing as a distinct  $\sim 80\text{ nm}$  thick band with moderate  $1656\text{ cm}^{-1}$  absorption and low reflectance, respectively. The stacking of the thylakoids is most apparent in the scattering amplitude image (Figure 4c). In contrast, phase imaging provides exceptional detail in the nuclear region allowing for clear differentiation of the nucleolus as well as a spherical nuclear body. A line profile across the nuclear body demonstrated both its particularly high absorption and its diameter of  $\sim 200\text{ nm}$  (Figure 4b insert). As such this nuclear body is likely a Cajal body [28].

The characteristic architecture of a eukaryotic flagellum can be seen in the axoneme. The scattering amplitude (Figure 4f) resolves the nine pairs of outer doublet microtubules and their radial spokes, while the central microtubules and the inner sheath can be seen as a slightly lower region of AFM topography (Figure 4d) in the center of the flagellum. The phase image in contrast, exhibits strong and homogeneous peptide absorption across the flagellum, and moderate absorption of the surrounding cell wall (Figure 4e). These observed flagella structures are highly comparable to previously reported *Chlamydomonas* flagellum characteristics [29].

The combination of AFM topography and sSNOM spectroscopy was also a valuable tool in the analysis of prokaryotic cells. *E. coli* cross sections (sectioned along either axis) were visually similar when comparing TEM and AFM imaging (Figure S1). Strong amide I and amide II bands are present throughout the cell with strong intracellular resin penetration (Figure S1c and d). Although an *E. coli* cell is approximately ten times smaller than a *C. reinhardtii* cell and does not contain internal membrane-bound vesicles, as evident from the AFM image (Figure S3 a), the resolving power of sSNOM imaging at  $1658\text{ cm}^{-1}$  clearly distinguishes several subcellular features. Overall, the cytoplasmic region shows strong absorption at this wavenumber (Figure S3b), but with an anisotropic distribution. A particularly dense region (suggesting high protein content) can be observed in the upper right of the cell. Conversely, there are several central patches of moderate to low amide I absorption. The sSNOM amplitude image is also anisotropic with similar regions varying in intensity (Figure S2c). The outer membrane has moderate amide I absorption and was used to determine a lateral resolution of  $\sim 20\text{ nm}$  of our sSNOM image recordings (Figures S3d).

### sSNOM tomography

Utilizing the top-view optics of the sSNOM imaging system, it was possible to identify several consecutive cross sections each from the same individual cell. Combining the sSNOM phase images of these ten consecutive, 100 nm thick cellular cross sections (Figure 5a) resulted in a  $1\text{ }\mu\text{m}$  thick 3D tomographic reconstruction (Figure 5b), representing approximately 10% of the entire cell. This tomograph provided a volumetric representation of the local intracellular protein distribution allowing for the 3D visualization of IR signatures of the membrane-bound organelles within a cell. The protein concentration within the pyrenoid is particularly high and as a result, the contrast in this region demonstrates the arrangement of the starch “fingers” within the pyrenoid. Similarly, the nuclear region also shows strong absorption, however, this dispersal in 3D space is more sporadic than in the pyrenoid. Conversely, the white and blue regions of lower absorption volumetrically represent the size, shape and distribution of the various cellular vacuoles across the cytoplasmic region of the cell. Thus, we infer that sSNOM tomography provides a direct chemical volumetric map at nm resolution where the contrast results from IR absorption.

## Discussion

Near-field nanoscopy was employed as a method to chemically image biological samples, specifically the internal cellular structures of both prokaryotic (*E. coli*) and eukaryotic (*C. reinhardtii*) model species.

NanoFTIR spectroscopy provided data from the mid-IR region, and sSNOM imaging was utilized to map this chemical data with a resolution well below the diffraction limit of about 5  $\mu\text{m}$ . The level of chemical detail achieved with sSNOM phase imaging goes beyond what is available through TEM, and is further supplemented by the simultaneously gathered AFM and sSNOM amplitude micrographs. Additionally, sSNOM phase imaging of several consecutive cross sections of a single cell allowed us to produce a 3D volumetric image of local intracellular protein distribution with dimensions of each voxel being 20 nm x 20 nm x 1  $\mu\text{m}$  corresponding to 400 zeptoliter ( $4 \times 10^{-19}$  l). The preparation of cellular samples by resin embedding and cross sectioning shown here, can be readily applied in photothermal-expansion microscopy, such as AFM-IR [30].

Nanoscale IR imaging and tomography is an attractive new approach to subcellular label-free imaging, which complements the growing arsenal of other super-resolution imaging modalities. One such complementary vibrational technique to IR nanoscopy is tip-enhanced Raman scattering (TERS). This technique can resolve single molecules [31]. Detection of vibrational spectra of biological samples (such as proteins and genetic material) is hampered by the weak Raman scattering cross section and the required high laser intensities may lead to sample damage. High-resolution TERS imaging of biological samples such as whole cells or cellular cross-sections at cryogenic temperatures and by using super-sharp tips, is an ongoing challenge [32].

Fluorescence microscopy offers excellent resolving power and can be employed to identify a multitude of cellular features, physiological properties and various metabolic activities, especially of living cells [33]. Fluorescence microscopy offers superior imaging contrast, yet fluorescence spectra are broad and the application of a number of dyes for spectral multiplexing is limited. Here, the vibrational spectra of biological samples provide a manifold of characteristic bands for multiplexing. Hyperspectral IR nanoscopy [34] is still in its infancy but technical progress in concert with the application of machine-learning and deep-learning algorithms is expected to provide unprecedented chemical contrast [35]. Unlike fluorescence-based super-resolution imaging techniques, sSNOM presents an approach to nanoscale chemical imaging that does not rely on the use of chemical labeling, and can be applied to samples under ambient conditions. While fluorescence emission degrades over time, IR spectroscopy is minimal invasive and the presented sample preparation method provides specimens that are stable over extended periods.

The spatial resolution in sSNOM is proportional to the AFM tip size. Thus, decreasing the apex radius directly improves the achievable resolution but on the expense of the reflected signal intensity. While sSNOM shows high sensitivity at high spatial resolution due to nonlinear dependence of the detected intensity on the near-field enhancement, the power dependence of the incident light is the same as in conventional far-field microscopy [36]. Conceptually, this relates to the modified Abbe's equation describing the diffraction limit where the intensity of the focal area in stimulated emission depletion (STED) microscopy is taken into account [37].

Through the combination of near-field spectroscopy and imaging, several specific inferences can be made about the examined samples. Phase-contrast imaging proved to be specifically useful in identifying areas of condensed protein or genetic material. For example, IR nanoscopy revealed regions likely to be rich in genetic material in both *E. coli* (Figure S2 c) and *C. reinhardtii* (Figure 3c and 4b). The Cajal body identified in *C. reinhardtii* (Figure 4b) is typically found in proliferating cells. Therefore, there is potential that sSNOM could be used to identify physiologically or metabolically active cells.

NanoFTIR spectroscopy of the inner cytoplasmic region of *C. reinhardtii* showed several areas of resin penetration, of which the spatial orientation was identified through sSNOM imaging. Resin in these areas suggests that water-soluble cellular components were replaced by resin during the embedding process. Furthermore, the distinct layered structure of the thylakoids was clearly resolved, but the chlorophyll peaks typical of chloroplasts, were not clearly distinguished in the nanoFTIR spectra due to rather low absorption intensity. This is not unexpected however, as samples require dehydration with alcohol prior to resin embedding, visibly leaching green pigments from the microalgae samples.

As such, the resin-embedding process may be introducing artifacts into the samples. However, current advances in IR nanoscopy could be integrated, further enhancing outputs and expanding operability into more biologically relevant conditions and more extreme environments. For instance, cryo-sectioning of samples would circumvent the need for resin embedding and performing sSNOM imaging under cryogenic conditions could increase sensitivity even further [38]. Additionally, sSNOM imaging has recently been performed on thin protein-rich membranes [39] and peptoid nanosheets [40] immersed in water, thus immensely opening up this technique to further bio imaging applications.

The IR tomographical technique described here can be expanded upon and potentially used alongside automation techniques typical for TEM tomography. The 3D chemical mapping of an entire cell and its substructures is a logical advance which could be adapted to studying even multicellular structures and tissue. We also envisage this method to be further applied to subcellular imaging, specifically investigating the function and structural details of individual cellular components through 3D visualization of IR absorption.

The potential spectroscopic information that can be gathered with this technique may be remarkably complex with a multitude of organic chemical groups contributing to the absorption in the IR region. Therefore, insights gathered via single-wavelength sSNOM imaging will be extremely valuable, furthering the possibility of deeply exploring the molecular composition of individual microorganisms and their subcellular components. In essence, super-resolution IR imaging and tomography provides a broad potential for major contributions to the field of subcellular biology including nanomedicine, nanotoxicology, disease-related imaging, diagnostics and therapy prediction.

## Methods

The green alga *C. reinhardtii* CC-125 (mt+) was cultured under constant illumination of 50  $\mu\text{mol photons m}^{-2} \text{ s}^{-1}$ , agitation of 110 rpm at 28 °C in Tris-Acetate-Phosphate medium [41]. *E. coli* K12 (DSM 498) was cultured with 110 rpm of agitation at 37 °C in Brain Heart Infusion Broth (Merck, Germany). After reaching log-phase growth, cultures were fixed in Cacodylate combination fixative (0.1 M Cacodylate buffer, 2% formaldehyde, 2.5% glutaraldehyde, 0.088 M sucrose, 0.001 M  $\text{CaCl}_2 \cdot \text{H}_2\text{O}$ , pH adjusted to 7.4; Merck, Germany) at room temperature for two hours. Following fixation, aliquots of each culture for TEM imaging were stained for 1 hour in 1% osmium tetroxide (diluted in 0.1 M Cacodylate buffer). All samples were dehydrated using an ethanol series from 50% – 100% (v/v), increasing in 10% increments and incubating at room temperature for 30 min at each concentration. Following the 100% ethanol incubation, each sample was resuspended twice in propylenoxid (Merck, Germany).

Samples were centrifuged for 3 min, 14,000 rcf, and the resulting pellet was maintained as well as possible during the resin-embedding process. Agar Low Viscosity Resin (Agar Scientific, UK) was prepared as per manufacturer's instructions, and then added to each sample at a 50% concentration (v/v in ethanol). Samples were incubated at room temperature overnight, in open vessels, to encourage evaporation. The resin concentration was then increased in 10% increments, incubating at room temperature for 30 min with each resin addition. Following an additional resuspension in 100% resin, samples were placed under vacuum for 30 min, before curing at 60 °C overnight.

Resin-embedded samples were cut to a thickness of 100 nm, using a microtome (Reichert ultracut S, Leica, Germany) fitted with a diamond knife (Histo 45°, DiATOME, USA). The ultrathin sections for TEM imaging were mounted on nickel square mesh grids (AGG2200N, Agar scientific, UK). These samples were subsequently stained with UranylLess (Delta Microscopies, France) for 2 min, followed by 3% Reynolds lead citrate (Delta Microscopies, France) for 2 min. To prevent precipitation of the lead citrate, pellets of NaOH were added to the staining chamber to exclude atmospheric  $\text{CO}_2$ . Samples were dried and washed at least three times with double distilled water after each step. TEM was performed using a JEM-1400Flash (JEOL, Japan). For image acquisition and processing, software provided by the TEM manufacturer was used (TEM Center 1.7.18.2349, 2006-20018 JEOL, Japan). The microscope was used with high voltage of 120 kV with a beam current of 60.80  $\mu\text{A}$ , while using a medium spot-size to reduce the risk of damaging the section. A 9x9 image montage was recorded at high magnification, and after brightness correction, was compiled into one stitched image.

Thin sections for AFM, nanoFTIR and sSNOM analysis were transferred to a flat template stripped gold (TS Au) surface. To prepare the TS Au surfaces [42], a 100 nm thick gold (99.999% Au, Kurt J. Lesker Company, Germany) layer was thermally evaporated onto a silicon wafer using physical vapor deposition (MBraun, Germany). Microscopy glass slides cut in  $\sim 1 \times 1$  cm pieces were glued on the Au surface using adhesive (NOA 81, Norland Products, USA) and cured with UV lamp. The glass pieces were then removed from the silicon surface and inverted to obtain a flat gold surface for sample deposition.

In order to gather consecutive cross sections for sSNOM tomographic analysis, prior to ultrathin sectioning, the resin-embedded samples were cut into trapezoidal shape, thus causing sequential thin

sections to adhere to the previous section, thus maintaining their orientation by forming a ribbon. This ribbon was then transferred to a TS Au surface as above.

An Atomic Force Microscope (NanoWizard II, JPK Instruments, Bruker Nano, Germany) was used for imaging of the thin sections under ambient conditions. The microscope was operated in tapping mode, using commercially available tips (Arrow NCPt, NanoWorld, Switzerland) with resonance frequency of 285 kHz. NanoFTIR spectroscopy was performed using a custom-built setup [14], equipped with broadband femtosecond laser source (FemtoFiber dichro midIR, NeaSpec, Germany). The sample side of the recorded interferograms was Fourier transformed to obtain the amplitude and phase spectra. Each spectrum represents an average of 50 co-additions measured at spectral resolution of  $16\text{ cm}^{-1}$ . For sSNOM imaging, a commercial system (neaSNOM, NeaSpec, Germany) with four quantum cascade laser chips (Daylight Solutions, USA) covering the mid-IR spectral region was used. The AFM and sSNOM images were visualized using Gwyddion (v. 2.51). 3D reconstruction and visualization was performed using Amira 6.3.0 (Avizo, ThermoFisher Scientific, Germany).

## Declarations

### Acknowledgments

This work has been funded by a grant from the German Research Foundation to J.H. (DFG, project HE 2063/5-1) and to D.J.N. (Emmy-Noether program, NU 421/1-1). A.E. was supported by the European Union's Horizon 2020 research and innovation program under the Marie Skłodowska-Curie grant agreement No. 706072 (NanoMemBR). D.J.B. and A.E. gratefully acknowledge funding by BMWi/DLR (grant number 50WB1623 and 50WB2023). A. E. acknowledges funding by Volkswagen Foundation and its Freigeist Program. The authors acknowledge support by the research building SupraFAB of Freie Universität Berlin.

### Author Contributions

The project idea was conceived and coordinated by A.E. and J.H. Microalgae cultures were provided by D.J.N. while sample preparation and resin embedding were performed by D.J.B. Microtomy and mounting of serial sections was performed by A.E. and D.J.B. AFM, nanoFTIR and sSNOM experiments were performed by K.K. Spectroscopic analysis was supported by J.H. 3D reconstruction was performed by K.K., and image interpretation was supported by D.J.B. and D.J.N. Counterstaining and TEM imaging was contributed by P.K.H. The manuscript was written by K.K., D.J.B. and J.H. with contributions by the other authors. All authors read and acknowledged the manuscript.

### Competing Interests Statement

none

## References

1. Yip, K.M., et al., *Atomic-resolution protein structure determination by cryo-EM*. Nature, 2020. **587**(7832): p. 157–161.
2. Sigal, Y.M., R. Zhou, and X. Zhuang, *Visualizing and discovering cellular structures with super-resolution microscopy*. Science, 2018. **361**(6405): p. 880–887.
3. Schermelleh, L., et al., *Super-resolution microscopy demystified*. Nat Cell Biol, 2019. **21**(1): p. 72–84.
4. Faist, J., et al., *Quantum cascade laser*. Science, 1994. **264**(5158): p. 553–6.
5. Kuepper, C., et al., *Quantum Cascade Laser-Based Infrared Microscopy for Label-Free and Automated Cancer Classification in Tissue Sections*. Sci Rep, 2018. **8**(1): p. 7717.
6. Cheng, J.X. and X.S. Xie, *Vibrational spectroscopic imaging of living systems: An emerging platform for biology and medicine*. Science, 2015. **350**(6264): p. aaa8870.
7. Betzig, E., et al., *Near Field Scanning Optical Microscopy (NSOM): Development and Biophysical Applications*. Biophys J, 1986. **49**(1): p. 269–79.
8. Kawata, S. and Y. Inouye, *Scanning probe optical microscopy using a metallic probe tip*. Ultramicroscopy, 1993. **57**: p. 313–317.
9. Mastel, S., et al., *Understanding the Image Contrast of Material Boundaries in IR Nanoscopy Reaching 5 nm Spatial Resolution*. ACS Photonics, 2018. **5**(8): p. 3372–3378.
10. Amarie, S. and F. Keilmann, *Broadband-infrared assessment of phonon resonance in scattering-type near-field microscopy*. Physical Review B, 2011. **83**(4).
11. Amenabar, I., et al., *Structural analysis and mapping of individual protein complexes by infrared nanospectroscopy*. Nat Commun, 2013. **4**: p. 2890.
12. Paulite, M., et al., *Imaging secondary structure of individual amyloid fibrils of a beta2-microglobulin fragment using near-field infrared spectroscopy*. J Am Chem Soc, 2011. **133**(19): p. 7376–83.
13. Kastner, B., et al., *Infrared Nanospectroscopy of Phospholipid and Surfactin Monolayer Domains*. ACS Omega, 2018. **3**(4): p. 4141–4147.
14. Mészáros, L., et al., *Spectroscopic investigations under whole cell conditions provide new insight into the metal hydride chemistry of [FeFe]-hydrogenase*. Chemical Science, 2020.
15. Hauer, B., A.P. Engelhardt, and T. Taubner, *Quasi-analytical model for scattering infrared near-field microscopy on layered systems*. Opt Express, 2012. **20**(12): p. 13173–88.
16. Zancajo, V.M.R., et al., *FTIR Nanospectroscopy Shows Molecular Structures of Plant Biominerals and Cell Walls*. Anal Chem, 2020. **92**(20): p. 13694–13701.
17. Keilmann, F., *Vibrational-infrared near-field microscopy*. Vibrational Spectroscopy, 2001. **29**: p. 109–114.
18. Taubner, T., R. Hillenbrand, and F. Keilmann, *Nanoscale polymer recognition by spectral signature in scattering infrared near-field microscopy*. Applied Physics Letters, 2004. **85**(21): p. 5064–5066.
19. Ocelic, N., A. Huber, and R. Hillenbrand, *Pseudoheterodyne detection for background-free near-field spectroscopy*. Applied Physics Letters, 2006. **89**(10).

20. Keilmann, F. and S. Amarie, *Mid-infrared Frequency Comb Spanning an Octave Based on an Er Fiber Laser and Difference-Frequency Generation*. Journal of Infrared, Millimeter, and Terahertz Waves, 2012. **33**(5): p. 479–484.
21. Huth, F., et al., *Nano-FTIR absorption spectroscopy of molecular fingerprints at 20 nm spatial resolution*. Nano Lett, 2012. **12**(8): p. 3973–8.
22. Salome, P.A. and S.S. Merchant, *A Series of Fortunate Events: Introducing Chlamydomonas as a Reference Organism*. Plant Cell, 2019. **31**(8): p. 1682–1707.
23. K. Kuchitsu, M.T.a.S.M., *Characterization of the Pyrenoid Isolated from Unicellular Green Alga Chlamydomonas reinhardtii: Particulate Form of RuBisCO Protein*. Protoplasma, 1988. **144**: p. 17–24.
24. Kuchitsu, K., M. Tsuzuki, and S. Miyachi, *Polypeptide Composition and Enzyme-Activities of the Pyrenoid and Its Regulation by Co2 Concentration in Unicellular Green-Algae*. Canadian Journal of Botany-Revue Canadienne De Botanique, 1991. **69**(5): p. 1062–1069.
25. Taillandier, E. and J. Liquier, *Infrared-Spectroscopy of DNA*. Methods in Enzymology, 1992. **211**: p. 307–335.
26. Han, Y., et al., *Key factors in FTIR spectroscopic analysis of DNA: the sampling technique, pretreatment temperature and sample concentration*. Analytical Methods, 2018. **10**(21): p. 2436–2443.
27. Katz, J.J., R.C. Dougherty, and L.J. Boucher, *7 - Infrared and Nuclear Magnetic Resonance Spectroscopy of Chlorophyll\*\*Based on work performed under the auspices of the U.S. Atomic Energy Commission*, in *The Chlorophylls*, L.P. Vernon and G.R. Seely, Editors. 1966, Academic Press. p. 185–251.
28. Cuevas-Velazquez, C.L. and J.R. Dinneny, *Organization out of disorder: liquid-liquid phase separation in plants*. Curr Opin Plant Biol, 2018. **45**(Pt A): p. 68–74.
29. Goodenough, U.W. and J.E. Heuser, *Substructure of inner dynein arms, radial spokes, and the central pair/projection complex of cilia and flagella*. J Cell Biol, 1985. **100**(6): p. 2008–18.
30. Dazzi, A., et al., *Local infrared microspectroscopy with subwavelength spatial resolution with an atomic force microscope tip used as a photothermal sensor*. Optics Letters, 2005. **30**(18): p. 2388–2390.
31. Lee, J., et al., *Visualizing vibrational normal modes of a single molecule with atomically confined light*. Nature, 2019. **568**(7750): p. 78–82.
32. Kurouski, D., et al., *Infrared and Raman chemical imaging and spectroscopy at the nanoscale*. Chem Soc Rev, 2020. **49**(11): p. 3315–3347.
33. Hell, S.W., et al., *The 2015 super-resolution microscopy roadmap*. Journal of Physics D: Applied Physics, 2015. **48**(44).
34. Amenabar, I., et al., *Hyperspectral infrared nanoimaging of organic samples based on Fourier transform infrared nanospectroscopy*. Nat Commun, 2017. **8**: p. 14402.

35. Pradhan, P., et al., *Deep learning a boon for biophotonics?* J Biophotonics, 2020. **13**(6): p. e201960186.
36. Atkin, J.M., et al., *Nano-optical imaging and spectroscopy of order, phases, and domains in complex solids.* Advances in Physics, 2012. **61**(6): p. 745–842.
37. Westphal, V. and S.W. Hell, *Nanoscale resolution in the focal plane of an optical microscope.* Phys Rev Lett, 2005. **94**(14): p. 143903.
38. Yang, H.U., et al., *A cryogenic scattering-type scanning near-field optical microscope.* Rev Sci Instrum, 2013. **84**(2): p. 023701.
39. Pfitzner, E. and J. Heberle, *Infrared Scattering-Type Scanning Near-Field Optical Microscopy of Biomembranes in Water.* J Phys Chem Lett, 2020. **11**(19): p. 8183–8188.
40. O'Callahan, B.T., et al., *In Liquid Infrared Scattering Scanning Near-Field Optical Microscopy for Chemical and Biological Nanoimaging.* Nano Lett, 2020. **20**(6): p. 4497–4504.
41. Donald S. Gorman, R.P.L., *Cytochrome F and Plastocyanin: their sequence in the photosynthetic electron transport chain of Chlamydomonas reinhardtii* Biochemistry, 1965. **54**.
42. Hegner, M., P. Wagner, and G. Semenza, *Ultralarge Atomically Flat Template-Stripped Au Surfaces for Scanning Probe Microscopy.* Surface Science, 1993. **291**(1–2): p. 39–46.

## Figures

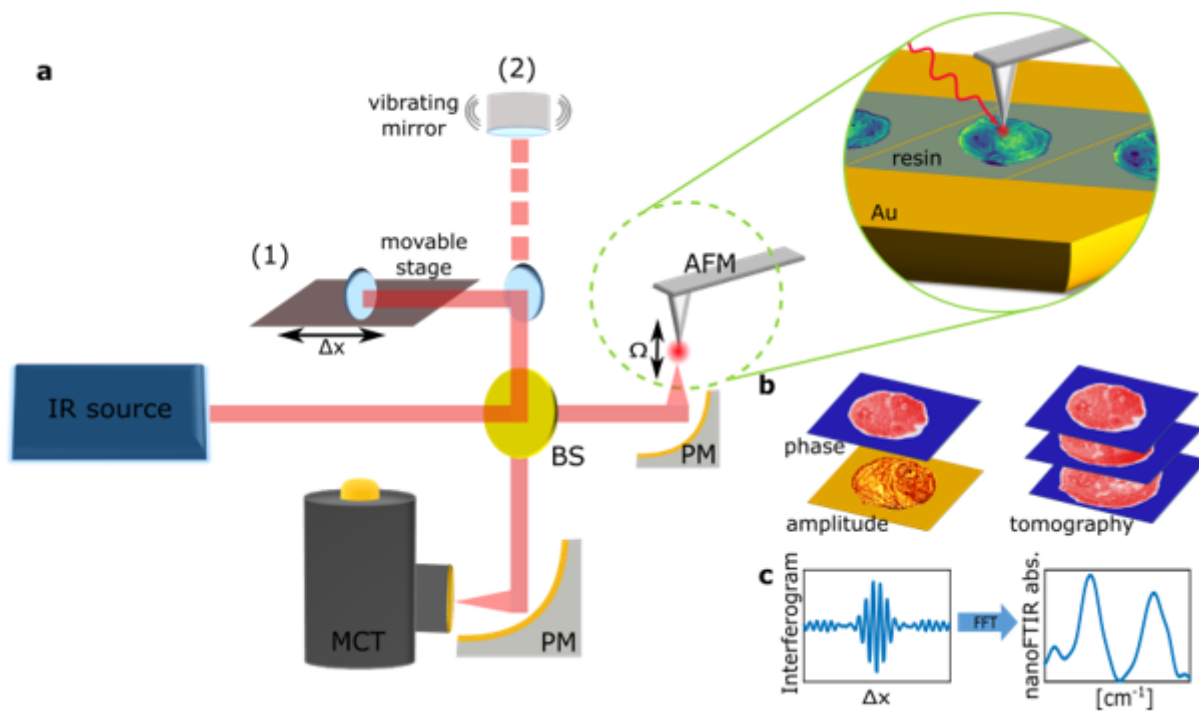


**Figure 1**

Operating modes of IR nanoscopy in an asymmetric Michelson interferometer scheme. (a) IR radiation, either broadband fs laser for nanoFTIR or QCL for sSNOM, is guided through a beamsplitter (BS) and

focused on an oscillating AFM tip via a parabolic mirror (PM). For nanoFTIR (1), the reference arm mirror is mounted on a movable stage. In sSNOM mode (2), the reference arm is equipped with piezo-driven mirror. The scattered light from the tip is recombined with the reflected light from the reference arm at the BS, focused on a mercury-cadmium-telluride (MCT) detector, and fed to a lock-in amplifier. (b) Simultaneously to AFM imaging, the demodulated sSNOM scattering amplitude and phase are recorded. sSNOM tomography is performed by imaging of serial sections. (c) The detected interferogram, demodulated at higher harmonics of the tip's resonance frequency  $\Omega$ , is Fourier transformed to obtain a near-field spectrum.

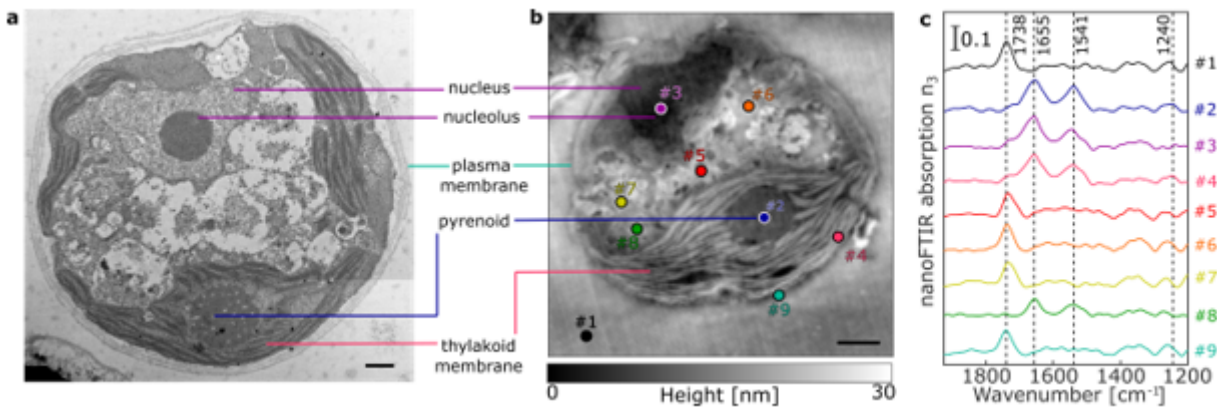


Figure 2

*C. reinhardtii* cross sections imaged by TEM (a) and AFM (b). Scale bars equal 1  $\mu\text{m}$ . nanoFTIR absorption spectra (c) were acquired at nine different locations marked on the AFM images.

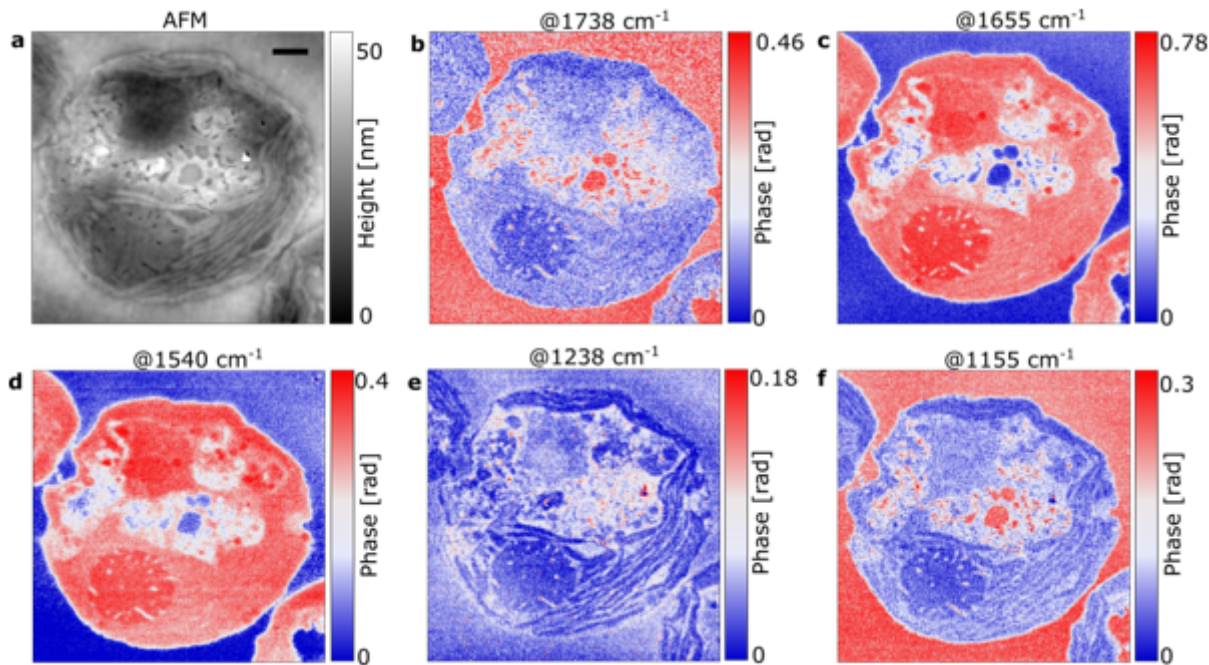
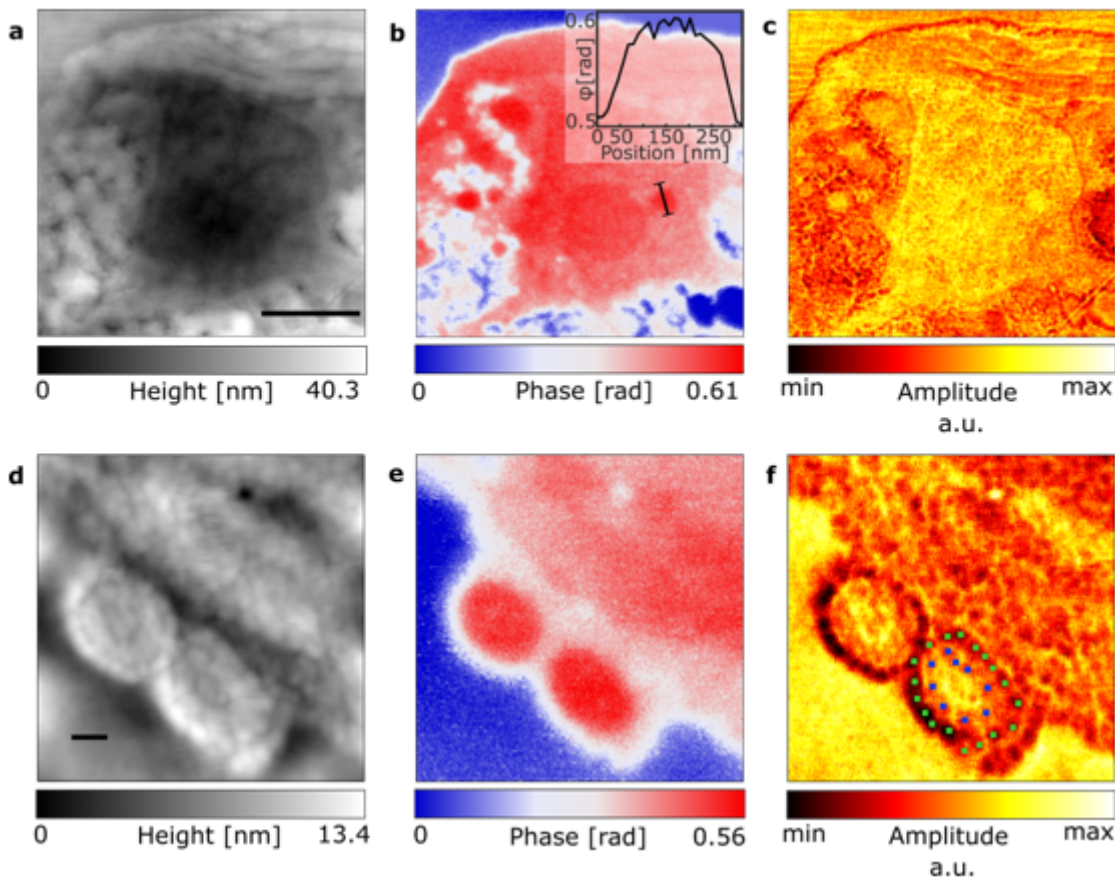


Figure 3

Cross section of a *C. reinhardtii* cell visualized by AFM topography (a) and sSNOM phase imaging at several wavenumbers (b-f), with red indicating high and blue indicating low absorption of each respective wavenumber. Scale bar equals 1  $\mu\text{m}$ .



**Figure 4**

Imaging of specific intracellular structures of a *C. reinhardtii* cell. The nuclear region is visualized by AFM topography (a) with the scale bar showing 1  $\mu\text{m}$ , sSNOM phase imaging (b) with the inset showing a line profile across a nuclear body, and sSNOM amplitude (c). The axoneme of the flagellum is similarly visualized using AFM topography (d) with the scale bar showing 100 nm, sSNOM phase imaging (e) and sSNOM amplitude (f), with the doublet microtubules (green marks) and the radial spokes (blue marks) of the flagellum. All sSNOM imaging was performed at 1656  $\text{cm}^{-1}$ .

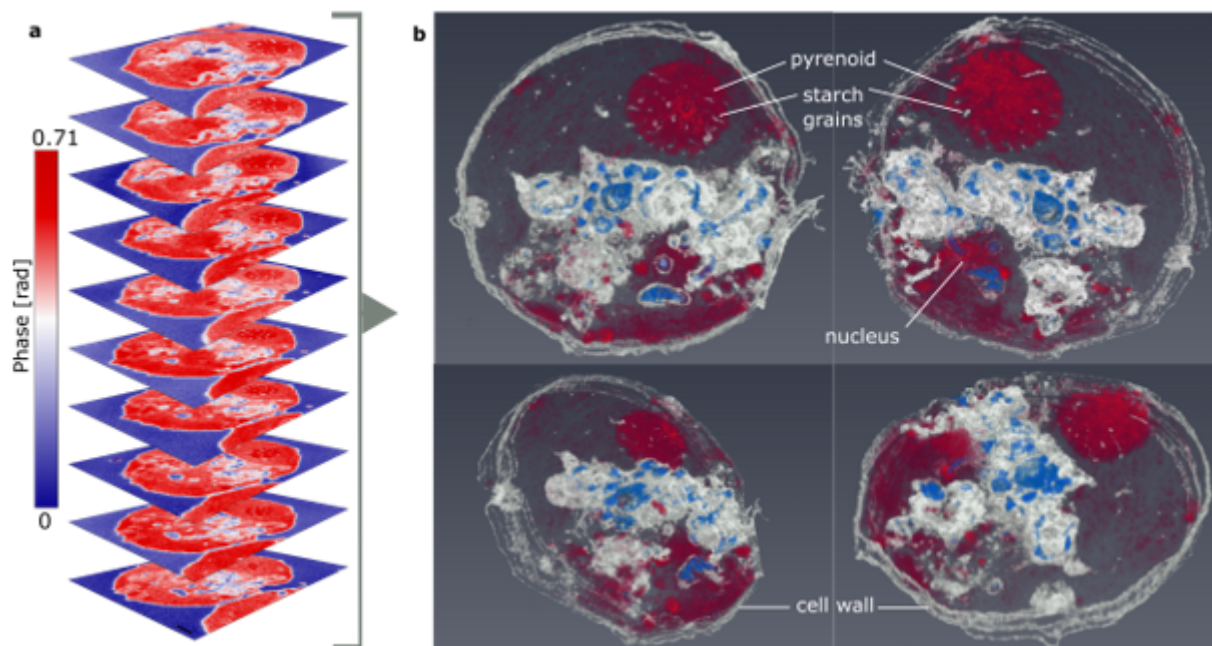


**Figure 5**

Ten consecutive sSNOM images of *C. reinhardtii*, recorded at 1656  $\text{cm}^{-1}$  (a) used for the construction of a tomogram (b), shown in four orientations: top right - view from the top, top left - view from the bottom, bottom left - top view tilted, bottom right - bottom view tilted (Supplementary video link).

## Supplementary Files

This is a list of supplementary files associated with this preprint. Click to download.

- [SupplementaryVideosSNOMtomography.mpg](#)
- [FigureS1.png](#)
- [FigureS2.png](#)
- [FigureS1.png](#)